Chinese Journal of Physics 65 (2020) 377–388

Contents lists available at ScienceDirect

Chinese Journal of Physics

journal homepage: www.elsevier.com/locate/cjph

Location impact of a pair of magnetic sources on melting of a magneto-Ferro phase change substance

Mohsen Izadi[a], Mohammad Ghalambaz[b,c,*], S.A.M. Mehryan[d]

[a] Mechanical Engineering Department, Faculty of Engineering, Lorestan University, Khorramabad, Iran
[b] Metamaterials for Mechanical, Biomechanical and Multiphysical Applications Research Group, Ton Duc Thang University, Ho Chi Minh City, Vietnam
[c] Faculty of Applied Sciences, Ton Duc Thang University, Ho Chi Minh City, Vietnam
[d] Young Researchers and Elite Club, Yasooj Branch, Islamic Azad University, Yasooj, Iran

ARTICLE INFO

Keywords:
Non-uniform magnetic field
Magnetic sources
Melting heat transfer
Latent thermal energy storage

ABSTRACT

The current numerical study aims to observe the location impact of a pair of magnetic sources on the melting rate of a magneto-ferro phase change substance in a cavity. The advanced moving mesh method is employed to model the phase change at an exact fusion temperature. The left and right walls of the enclosure are subject to the higher and lower temperatures, respectively. Two other walls are kept insulated. The pair of the non-uniform magnetic fields are located in the vicinity of the walls of the enclosure. Galerkin finite element method is employed to obtain the numerical results. The Arbitrary Lagrangian–Eulerian (ALE) deformed mesh technique allowing deformation of the interface of the molten and non-molten regions is set up. The outcomes demonstrate the dependency of the progress of the melting front to the location of the sources. When the pair of sources are placed in the vicinity of the cold wall, the melting rate is higher. On the other hand, the final time of the melting process is almost the same for the cases with the sources placed in the adjacent of the cold left and insulated bottom walls.

1. Introduction

It is widely believed that exploring alternatives to fossil fuels is of vital importance for our future life on earth. Over the years, this belief has been the impetus behind many scientific efforts to enhance our ability to harvest and exploit renewable and clean energies. Energy storage technologies play a central and inevitable role in the use of renewable energies such as solar and wind, as they are essential for managing the time differences between when these energies are needed (demand) and when they are available for efficient harvesting (supply).

One way to manage the aforementioned time-gap between supply and demand is to use thermal energy storage solutions. These solutions can function based on latent heat, sensible heat, thermochemical heat, or a combination of these concepts. In the sensible heat approach, thermal energy is stored by raising the temperature of matter, but in the latent heat method, energy is stored through a change in the phase of matter. Thermochemical energy storage systems function based on the energy released when chemical bonds break down or change form during a reaction.

Among the above approaches, latent heat storage with phase change materials (PCMs) is the most sensible option, as they are perfect for storing and releasing energy at a constant temperature. PCMs are materials with a high latent heat of fusion, convenient

---

[*] Corresponding author.
E-mail addresses: izadi.m@lu.ac.ir (M. Izadi), mohammad.ghalambaz@tdtu.edu.vn (M. Ghalambaz).

https://doi.org/10.1016/j.cjph.2020.03.002
Received 11 January 2020; Received in revised form 17 February 2020; Accepted 3 March 2020

Nomenclature

Latin symbols

B	magnetic induction vector (T)
c_p	specific heat capacity (J kg^{-1} K^{-1})
Ec	Eckert number
Fo	Fourier number
F_B	bouyancy force (N)
F_K	kelvin force (N)
F_L	lorentz force (N)
G	magnetic field strength (A m^{-1})
G_x, G_y	components of magnetic field strength along x, y directions, respectively (A m^{-1})
g	acceleration of gravity vector (m s^{-2})
Ha	Hartmann number
k	thermal conductivity (W m^{-1} K^{-1})
K	permeability of the porous medium (m^2)
L	characterization length (m)
M	magnetization (A m^{-1})
Mn_f	Magnetic number
M_x, M_y	components of the magnetization vector along x, y directions, respectively (Am^{-1})
p	dimensional pressure of the liquid PCM (Pa)
P	non-dimensional pressure of the liquid PCM
Pr	Prandtl number
Q	total heat generation (J)
Q_J	joule heating (J)
Q_M	magnetocaloric heating (J)
Ra	Rayleigh number
Ste	Stefan number
t	dimensional time (s)
T	temperature field (K)
T_{Cur}	Curie temperature (K)
$\boldsymbol{u}$	velocity vector (m s^{-1})
u, v	components of velocity vector along x, y directions, respectively (m s^{-1})
U, V	Components of the dimensionless velocity vector along X, Y directions, respectively
x, y	Cartesian coordinates (m)
x_1, y_1	dimensional location of the magnetic source 1 (m)
x_2, y_2	dimensional location of the magnetic source 2 (m)
X, Y	dimensionless Cartesian coordinates
X_1, Y_1	dimensionless location of the magnetic source 1
X_2, Y_2	dimensionless location of the magnetic source 2

Greek symbols

α	effective thermal diffusivity (m^2 s^{-1})
β	thermal expansion coefficient of the fluid (K^{-1})
γ	magnetic intensity (A m^{-1})
ε_1	Temperature number
θ	dimensionless temperature
μ	dynamic viscosity (kg m^{-1} s^{-1})
μ_0	magnetic permeability in vacuum (T m A^{-1})
ρ	density (kg m^{-3})
χ	penalty number
Ψ	dimensionless stream function

Subscripts

c	cold
f	fusion
h	hot
lp	liquid PCM
sp	solid PCM
w	wall

phase-change temperatures, and small volume changes during phase change, which make them a natural choice for thermal energy storage.

Cavities and channels with various geometries act as enclosure systems for variety of practical applications such as shock generators [1], supersonic mixing jets [2], heat exchangers [3], and heatsinks [4]. The heat transfer of free convection in an enclosure cavity has been also investigated in many recent studies by considering magneto-convection [5], magneto-hydrodynamic flows [6,7], nanofluids [8,9], hybrid nanofluids [10], non-Newtonian fluids [11], conjugate heat transfer [12,13], entropy generation [14], and porous media [15].

Energy storage with PCMs is an extensively researched subject. Abhat et al. [16] were the first to study the thermophysical properties of PCMs, such as thermal conductivity, specific heat, latent heat, and melting point. In research by Ho and Lin [17], the authors found that melting takes place faster in a cylindrical space with a larger radius ratio in the presence of a solid interface. Agarwal et al. [18] compared the impact of longitudinal and circular fins on the melting process and reported that fins accelerate the melting. In two studies by Tiari et al. [19,20]; it was shown that fin geometry plays an effective role in overall system performance. Kumar et al. [21] showed that the effect of buoyancy force on the melting process at high Rayleigh numbers could not be ignored. Sheikholeslami et al. [22] addressed the entropy generation of nano-enhanced phase change materials in a cavity during a charging process.

Given the low thermal conductivity of PCMs, scientists have been trying to solve this problem by adding nanoparticles to these materials. In this area, Khodadadi and Hosseinizadeh [23] reported that adding higher amounts of nanoparticles to PCMs reduced the discharge time. In another study, Hosseinizadeh et al. [24] reported that the melting rate of PCMs increased with the increase in their thermal conductivity and the decrease in their latent heat of fusion. Motahar et al. [25] investigated the effect of adding nanoparticles in different volume percentages on thermal conductivity and viscosity of PCMs at different temperatures. They also repeated the same experiments for oxy-silica nanoparticles [26]. The impact of using nanoparticles and metal foams for improvement of PCM was also addressed by Li et al. [27]. Using 5% of nanoparticles reduced the melting time by 25.9%.

As mentioned, Latent Heat Thermal Storage systems (LHTS) are likely to play a key role in future energy management. In an experimental study by Mahdi et al. [28], they investigated the performance of a spiral LHTS system in both melting and freezing processes. In these experiments, which were conducted with water and paraffin used as heat transfer fluid and PCM, respectively, they obtained the optimum flow rate of the heat transfer fluid in the melting process and reported that this rate is inconsequential in the freezing process. Ebrahimi et al. [29] studied the melting of PCMs with U-shaped tubes containing hot fluid in a heat exchanger. The results of this study showed that placing the tubes around the shell reduced the total melting time by 91%. Siyabi et al. [30] studied the effect of the rotation angle of the thermal storage unit on the melting process. This study found that using a rotation angle of 45° results in faster melting than other angles. Research by Mahdi et al. [31] assessed the thermal performance of a double-tube LHTS system with PCM placed in the central tube or the annular tube. This research showed that PCM froze faster when it was placed in the annular tube. In an attempt to enhance the thermal performance of solar energy storage units, Chen et al. [32] used a two-stage method for adding CuO nanoparticles to paraffin to produce a series of high-performance hybrid PCMs for efficient conversion and storage of solar thermal energy. Alva et al. [33] also introduced a series of materials that can be used in solar energy storage and related systems.

Several studies have reported that magnetic fields in residential and industrial spaces can affect natural convection [34–40]. A review of the literature shows that research on the effect of non-uniform magnetic fields on the charging (melting) process of LHTS systems has been scarce.

The present study investigated the effect of positioning of magnetic sources (four positions) on the melting process in a rectangular enclosure. The effects of both Lorentz forces due to the existence of a magnetic field and Kelvin force due to the non-uniform field on the melting process were studied. In this study, it was assumed that the hot water coming from the solar collector passes over the vertical wall of the energy storage unit and the position of magnetic sources was defined relative to the unit.

2. Physical model and computational domain

Fig. 1 indicates a two-dimensional schematic of the geometry under consideration. The enclosure is occupied by a solid PCM with the fusion temperature of T_f. The left and right walls are kept at higher and lower temperatures of T_h and T_c, while the two other bounds are insulated. The molten substance flowing in the enclosure acts as a Newtonian and laminar fluid. The enclosure domain is influenced by the gravitational and magnetic forces. Two magnetic sources, with the strength of γ, are placed in (x_1, y_1) and (x_1, y_2). The magnetic fields vectors applied are [41]:

$$\begin{bmatrix} \boldsymbol{G}_1^* \\ \boldsymbol{G}_2^* \end{bmatrix} = \begin{bmatrix} G_{1x}^* & G_{1y}^* \\ G_{2x}^* & G_{2y}^* \end{bmatrix} \begin{bmatrix} i \\ j \end{bmatrix} = \frac{\gamma}{2\pi} \begin{bmatrix} -\dfrac{(y_1-y)}{(y_1-y)^2+(x_1-x)^2} & \dfrac{(x_1-x)}{(y_1-y)^2+(x_1-x)^2} \\ -\dfrac{(y_2-y)}{(x_1-x)^2+(y_2-y)^2} & \dfrac{(x_1-x)}{(x_1-x)^2+(y_2-y)^2} \end{bmatrix} \begin{bmatrix} i \\ j \end{bmatrix} \tag{1}$$

Then, the total vector and scalar fields are

$$\boldsymbol{G}^* = \boldsymbol{G}_1^* + \boldsymbol{G}_2^* = G_x^* i + G_y^* j,\; G^* = \left(G_x^{*^2} + G_y^{*^2} \right)^{0.5} \tag{2}$$

The continuity equation of the molten substance in the computational domain is [42]:

$$\nabla \cdot \boldsymbol{u} = 0 \tag{3}$$

The momentum equation of the molten substance in the domain is defined as [42]:

$$\rho_{lp}\left(\frac{\partial \boldsymbol{u}}{\partial t} + \boldsymbol{u} \cdot \nabla \boldsymbol{u} \right) = -\nabla p + \nabla \cdot (\nabla \mu_{lp} \boldsymbol{u}) + \boldsymbol{F} \tag{4}$$

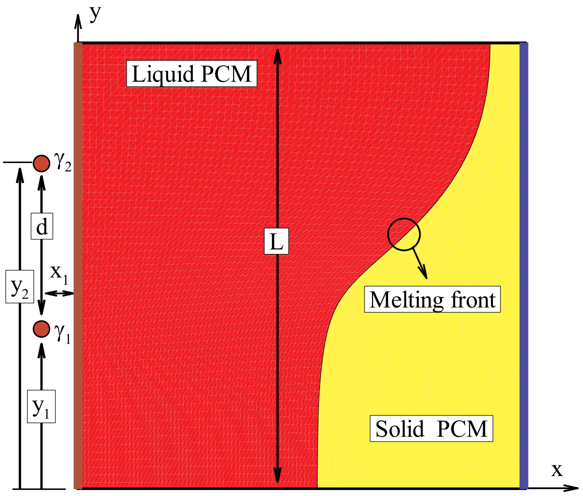

Fig. 1. Schematic picture of the considered problem.

in which $\boldsymbol{F}$ is:

$$\begin{aligned} \boldsymbol{F} &= \boldsymbol{F}_{\mathbf{L}} + \boldsymbol{F}_{\mathbf{B}} + \boldsymbol{F}_{\mathbf{K}} \\ \boldsymbol{F}_{\mathbf{L}} &= \boldsymbol{J} \times \boldsymbol{B} | \boldsymbol{J} = \sigma_{lp} \boldsymbol{u} \times \boldsymbol{B} \;\&\; \boldsymbol{B} = \mu_0 \boldsymbol{G}^* \\ \boldsymbol{F}_B &= \rho_{lp} \mathbf{g} \beta_{lp} (T - T_f) \\ \boldsymbol{F}_K &= \mu_0 (\boldsymbol{M} \cdot \nabla) \boldsymbol{G}^* | \boldsymbol{M} = M_x i + M_y j, \;\; M_x = M_y = K' G^* (T_{Cur} - T) \end{aligned} \tag{5}$$

Energy equation of the liquid PCM [41]:

$$(\rho c_p)_{lp} \left(\frac{\partial T}{\partial t} + \boldsymbol{u}.\, \nabla T \right) = \nabla \cdot (\nabla k_{lp} T) + Q \tag{6}$$

where

$$Q = Q_J + Q_M \left| \begin{array}{l} Q_J = \sigma_{lp} (u B_y - v B_x)^2 \\ Q_M = \mu_0 T \frac{\partial M}{\partial T} \left(u \frac{\partial G^*}{\partial x} + v \frac{\partial G^*}{\partial y} \right) \end{array} \right. \tag{7}$$

Energy equation of the solid PCM [42]:

$$(\rho c_p)_{sp} \frac{\partial T}{\partial t} = \nabla \cdot (\nabla k_{sp} T) \tag{8}$$

The initial and boundary conditions of the computational regions are as follows:

$$\text{On the left wall:} u = v = 0,\ T = T_h \tag{9-a}$$

$$\text{On the right wall:} u = v = 0,\ T = T_c \tag{9-b}$$

$$\text{On the lower and upper walls:} u = v = 0,\ \partial T / \partial y = 0 \tag{9-c}$$

$$\text{Initial condition:} u = v = 0,\ T = T_0 \tag{9-d}$$

Stefan condition describing the motion of boundary between the fluid and solid phases of the PCM is [43]:

$$u = \left(k_{lp} \frac{\partial T}{\partial x} \bigg|_{lp} - k_{sp} \frac{\partial T}{\partial x} \bigg|_{sp} \right) / (\rho_{lp} h_{sl}) \tag{10-a}$$

$$v = \left(k_{lp} \frac{\partial T}{\partial y} \bigg|_{lp} - k_{sp} \frac{\partial T}{\partial y} \bigg|_{sp} \right) / (\rho_{lp} h_{sl}) \tag{10-b}$$

We used the dimensionless parameters expressed below to parametrize and simplify the problem:

$$\begin{aligned} &X = \tfrac{x}{L}, \quad Y = \tfrac{y}{L}, \quad U = \tfrac{uL}{\alpha_{lp}}, V = \tfrac{vL}{\alpha_{lp}}, \quad \theta = \tfrac{T - T_c}{T_h - T_c}, \;\; P = \tfrac{L^2 p}{\rho \alpha_{lp}^2}, \\ &G = \tfrac{G^*}{G_0^*}, \quad G_X = \tfrac{G_X^*}{G_0^*}, \quad G_Y = \tfrac{G_y^*}{G_0^*}, Fo = \tfrac{t \alpha_{lp}}{L^2} \end{aligned} \tag{11}$$

where $G_0^* = \gamma / 2\pi L$. We then have:

$$\frac{\partial U}{\partial X} + \frac{\partial V}{\partial Y} = 0 \tag{12}$$

$$\begin{aligned} &\tfrac{\partial U}{\partial Fo} + U \tfrac{\partial U}{\partial X} + V \tfrac{\partial U}{\partial Y} = -\tfrac{\partial P}{\partial X} + Pr \left(\tfrac{\partial^2 U}{\partial X^2} + \tfrac{\partial^2 U}{\partial Y^2} \right) \\ &- Ha^2 Pr G_Y (U G_Y - V G_X) - Mn_f Pr \theta G \tfrac{\partial G}{\partial X} \end{aligned} \tag{13}$$

$$\begin{aligned} &\tfrac{\partial V}{\partial Fo} + U \tfrac{\partial V}{\partial X} + V \tfrac{\partial V}{\partial Y} = -\tfrac{\partial P}{\partial Y} + Pr \left(\tfrac{\partial^2 V}{\partial X^2} + \tfrac{\partial^2 V}{\partial Y^2} \right) + Ra Pr \theta \\ &- Ha^2 Pr G_X (V G_X - U G_Y) - Mn_f Pr \theta G \tfrac{\partial G}{\partial Y} \end{aligned} \tag{14}$$

The energy equation of the molten matter:

$$\begin{aligned} &\tfrac{\partial \theta}{\partial Fo} + U \tfrac{\partial \theta}{\partial X} + V \tfrac{\partial \theta}{\partial Y} = \left(\tfrac{\partial^2 \theta}{\partial X^2} + \tfrac{\partial^2 \theta}{\partial Y^2} \right) + Ec Ha^2 (U G_Y - V G_X)^2 \\ &+ Mn_f Ec G (\varepsilon_1 + \theta) \left(U \tfrac{\partial G}{\partial X} + V \tfrac{\partial G}{\partial Y} \right) \end{aligned} \tag{15}$$

The energy equation of the non-molten matter:

$$\frac{\partial\theta}{\partial Fo}=\left(\frac{\partial^2\theta}{\partial X^2}+\frac{\partial^2\theta}{\partial Y^2}\right) \tag{16}$$

where

$$\begin{aligned}&Ra=\frac{g\beta_{lp}\Delta TL^3}{\mu_{lp}\alpha_{lp}},\ Pr=\frac{\upsilon_{lp}}{\alpha_{lp}},\ Ha=\mu_0G_0L\sqrt{\frac{\sigma_{lp}}{\mu_{lp}}}\\&Ec=\frac{\mu_{lp}\alpha_{lp}}{\rho_{lp}c_{p,lp}\Delta TL^2},\ Mn_f=\frac{\mu_0G_0^{*2}K'\Delta TL^2}{\mu_{lp}\alpha_{lp}}\end{aligned} \tag{17}$$

In this study, the cold and Curie temperatures are considered to be the same. Also, the strength components of the magnetic field dimensionally are written as

$$\begin{aligned}&G_X=\frac{(Y-Y_1)}{(X-X_1)^2+(Y-Y_1)^2}+\frac{(Y-Y_2)}{(X-X_1)^2+(Y-Y_2)^2}\\&G_Y=-\frac{(X-X_1)}{(X-X_1)^2+(Y-Y_1)^2}-\frac{(X-X_1)}{(X-X_1)^2+(Y-Y_2)^2}\end{aligned} \tag{18}$$

The boundary and initial conditions in dimensionless coordinates are

On the left wall: $U=V=0,\ \ \theta=1$ (19-a)

$On the right wall\ U=V=0,\ \theta=0$ (19-b)

On the lower and upper walls: $U=V=0,\ \ \partial\theta/\partial Fo=0$ (19-c)

Initial condition: $U=V=0,\ \ \theta=\theta_0$ (19-d)

Besides, the dimensionless Stefan condition can be defined as:

$$U=Ste\left(\left.\frac{\partial\theta}{\partial X}\right|_{lp}-\left.\frac{\partial\theta}{\partial X}\right|_{sp}\right) \tag{20-a}$$

$$V=Ste\left(\left.\frac{\partial\theta}{\partial Y}\right|_{lp}-\left.\frac{\partial\theta}{\partial Y}\right|_{sp}\right) \tag{20-b}$$

which *Ste*, Stefan number, is defined as follows:

$$Ste=\frac{c_{p,lp}(T_h-T_f)}{h_{sl}} \tag{21}$$

3. Numerical approach and verification

3.1. Numerical approach

To solve the Eqs. (12)– (16) along with the appropriate initial and boundary conditions, the finite element method is employed. The weak form of the equations can be obtained using Galerkin weighted residual formulation which can be seen in details in [44]. Using a penalty function defined below, the pressure variable can be removed from the momentum equation:

$$P=\chi\left(\frac{\partial U}{\partial X}+\frac{\partial V}{\partial Y}\right) \tag{22}$$

The high values of penalty number, i.e. χ, can establish the mass conservation equation. Combination of the above-expressed equation and momentum equation results in the equations mentioned below:

$$\begin{aligned}&\frac{\partial U}{\partial Fo}+U\frac{\partial U}{\partial X}+V\frac{\partial U}{\partial Y}=-\frac{\partial}{\partial X}\left(\chi\left(\frac{\partial U}{\partial X}+\frac{\partial V}{\partial Y}\right)\right)+Pr\left(\frac{\partial^2U}{\partial X^2}+\frac{\partial^2U}{\partial Y^2}\right)\\&-Ha^2PrG_Y(UG_Y-VG_X)\end{aligned} \tag{23-a}$$

$$\begin{aligned}&\frac{\partial V}{\partial Fo}+U\frac{\partial V}{\partial X}+V\frac{\partial V}{\partial Y}=-\frac{\partial}{\partial Y}\left(\chi\left(\frac{\partial U}{\partial X}+\frac{\partial V}{\partial Y}\right)\right)+Pr\left(\frac{\partial^2V}{\partial X^2}+\frac{\partial^2V}{\partial Y^2}\right)\\&-Ha^2PrG_X(VG_X-UG_Y)+RaPr\theta\end{aligned} \tag{23-b}$$

U, V, and *T* can be expanded by utilizing a interpolation set $\{\xi_e\}_{e=1}^{N}$:

$$\theta\approx\sum_{e=1}^{N}\theta_e\xi_e(X,Y),\ \ V\approx\sum_{e=1}^{N}V_e\xi_e(X,Y),\ U\approx\sum_{e=1}^{N}U_e\xi_e(X,Y) \tag{24}$$

N appeared in the above expansions is the total grids number of the variables. Applying the Galerkin finite element technique to the equations leads to the following residuals:

$$
\begin{aligned}
R_i^1 \approx & \sum_{e=1}^{N} U_e \int \frac{\partial \xi_e}{\partial Fo}\xi_i dXdY + \sum_{e=1}^{N} U_e \int \left[\left(\sum_{e=1}^{N} U_e \xi_e\right)\frac{\partial \xi_e}{\partial X} + \left(\sum_{e=1}^{N} V_e \xi_e\right)\frac{\partial \xi_e}{\partial Y}\right]\xi_i dXdY \\
& + \gamma \left[\sum_{e=1}^{N} U_e \int \frac{\partial \xi_i}{\partial X}\frac{\partial \xi_e}{\partial X} dXdY + \sum_{e=1}^{N} V_e \int \frac{\partial \xi_i}{\partial X}\frac{\partial \xi_e}{\partial Y} dXdY \right] \\
& + Pr \sum_{e=1}^{N} U_e \int \left[\frac{\partial \xi_i}{\partial x}\frac{\partial \xi_e}{\partial x} + \frac{\partial \xi_i}{\partial y}\frac{\partial \xi_e}{\partial y} \right] dXdY + PrHa^2 G_Y^2 \int \left(\sum_{e=1}^{N} U_e \xi_e\right)\xi_i dXdY \\
& - PrHa^2 G_X G_Y \int \left(\sum_{e=1}^{N} V_e \xi_e\right)\xi_i dXdY
\end{aligned} \tag{25-a}
$$

$$
\begin{aligned}
R_i^2 \approx & \sum_{e=1}^{N} V_e \int \frac{\partial \xi_e}{\partial Fo}\xi_i dXdY + \sum_{e=1}^{N} V_e \int \left[\left(\sum_{e=1}^{N} U_e \xi_e\right)\frac{\partial \xi_e}{\partial x} + \left(\sum_{e=1}^{N} V_e \xi_e\right)\frac{\partial \xi_e}{\partial y}\right]\xi_i dXdY \\
& + \gamma \left[\sum_{e=1}^{N} U_e \int \frac{\partial \xi_i}{\partial y}\frac{\partial \xi_e}{\partial x} dXdY + \sum_{e=1}^{N} V_e \int \frac{\partial \xi_i}{\partial y}\frac{\partial \xi_e}{\partial y} dXdY \right] \\
& + Pr \sum_{e=1}^{N} V_e \int \left[\frac{\partial \xi_i}{\partial X}\frac{\partial \xi_e}{\partial X} + \frac{\partial \xi_i}{\partial Y}\frac{\partial \xi_e}{\partial Y} \right] dXdY - RaPr \int \left(\sum_{e=1}^{N} \theta_e \xi_e\right)\xi_i dXdY \\
& + PrHa^2 G_X^2 \int \left(\sum_{e=1}^{N} V_e \xi_e\right)\xi_i dXdY - PrHa^2 G_X G_Y \int \left(\sum_{e=1}^{N} U_e \xi_e\right)\xi_i dXdY
\end{aligned} \tag{25-b}
$$

$$
\begin{aligned}
R_i^3 \approx & \sum_{e=1}^{N} \theta_e \int \frac{\partial \xi_e}{\partial Fo}\xi_i dXdY + \sum_{e=1}^{N} \theta_e \int \left[\left(\sum_{e=1}^{N} U_e \xi_e\right)\frac{\partial \xi_e}{\partial x} + \left(\sum_{e=1}^{N} V_e \xi_e\right)\frac{\partial \xi_e}{\partial Y}\right]\xi_i dXdY \\
& + \sum_{e=1}^{N} \theta_e \int \left[\frac{\partial \xi_i}{\partial X}\frac{\partial \xi_e}{\partial X} + \frac{\partial \xi_i}{\partial Y}\frac{\partial \xi_e}{\partial Y} \right] dXdY - EcHa^2 \left(G_Y \int \left[\sum_{e=1}^{N} U_e \xi_e\right] - G_X \int \left[\sum_{e=1}^{N} V_e \xi_e\right]\right)^2 \xi_i dXdY
\end{aligned} \tag{25-c}
$$

3.2. *Grid test and verification*

The simulation accuracy is significantly affected by the meshing grid size. Furthermore, the divergence and convergence of the calculations can also be influenced by the grid size. A mesh consisting of structured quadratic elements were utilized to discretize the domain of the molten matter. While the elements of the non-molten region are unstructured triangular.

Theoretically, a mesh of a high number of elements can guarantee more accurate results. However, this mesh also leads to longer calculation time and higher memory usage. Therefore, finding an optimum mesh is necessary. Table 1 and Fig. 2 depict the result of the grid independence study. Several meshes of different sizes are investigated to obtain the optimum case. The analysis of the mesh density sensitivity and required run time, presented in Table 1 and Fig. 2, indicates that the number of elements of case 2 is quite enough for extracting the numerical outcomes. The test was performed for $Ha = 10$, $Ra = 2.1 \times 10^5$, $Mn_f = 10$, $Ste = 0.039$, $\varepsilon_1 = 0.0$, $Pr = 0.021$, $Y_1 = 0.3$, $Y_2 = 0.7$, $X_1 = X_2 = 0.05$, and $Ec = 10^{-6}$.

Ultimately, the validation of the computational model was obtained against several experimental and numerical works [45–48]. Fig. 3 illustrates the simulation of isotherms in the enclosure filled by a magnetic fluid against the presented outcomes by Sathiyamoorthy and Chamkha [45]. In the works reported in [46–48], the PCM melting of a non-magnetic matter in a rectangular cavity was studied. Fig. 4 reports the progress of the melting front at different Fourier numbers. In general, the excellent accuracies achieved as depicted in Figs. 3 and 4 indicate good validations of the used model in the current study for simulating the PCM melting and its natural convection.

4. Results and discussion

The impact of the position of the magnetic sources on the PCM melting in a thermal storage unit was studied. Fig. 5 illustrates the magnetic field applied from four different positions to the melting process in the thermal storage unit. The results are reported for the following set of non-dimensional parameters $Ha = 10$, $Ra = 2.1 \times 10^5$, $Mn_f = 10$, $Ste = 0.039$, $\varepsilon_1 = 0.0$, $Pr = 0.021$, $Y_1 = 0.3$, $Y_2 = 0.7$, $X_1 = X_2 = 0.05$, and $Ec = 10^{-6}$.; otherwise, the value of a parameter will be stated.

Fig. 6 displays the streamlines and isotherms that emerge in the four defined cases over time. As is clearly shown, the position of the magnetic sources relative to the unit has a significant impact on the melting process. It can be seen that the melting is faster when the magnetic sources are positioned on the right-side vertical wall or the bottom horizontal wall. It seems that in Case 1, the magnetic field is concentrated near the left-side wall and weakens the buoyancy forces near the hot wall. Therefore, there is more resistance to natural convection, and melting takes place at a slower pace. In Case 2, the impact of Lorentz forces shifts the central eddy downward, thus weakening the melting process in the upper area of the enclosure.

In contrast, as illustrated in Fig. 6c (the third row of Fig. 6), placing the magnetic sources on the right-side wall reduces the intensity of Lorentz forces applied to the fluid particles, leads to stronger streamlines and therefore enhanced convection and faster

Table 1
The number of utilized elements for discretizing the solid and liquid subdomains.

Cases	Case 1	Case 2	Case 3	Case 4
Grid size in solid region	560	974	1412	1868
Grid size in liquid region	30 × 30	60 × 60	90 × 90	120 × 120
Run time	18 min	1 h, 9 min	2 h, 44 min	5 h, 22 min

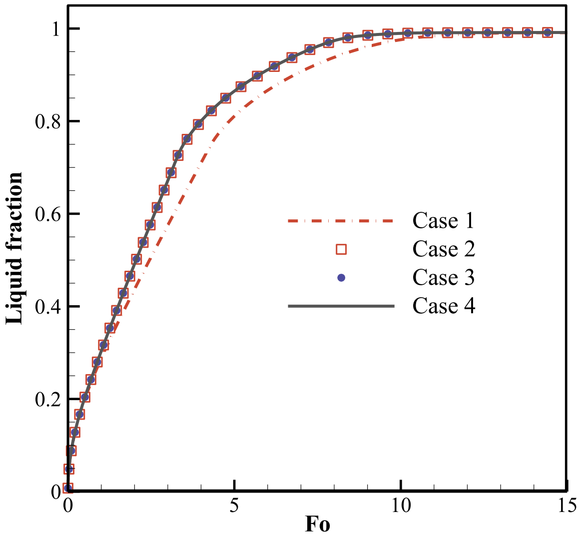

Fig. 2. Grid independency for the liquid fraction of the molten PCM.

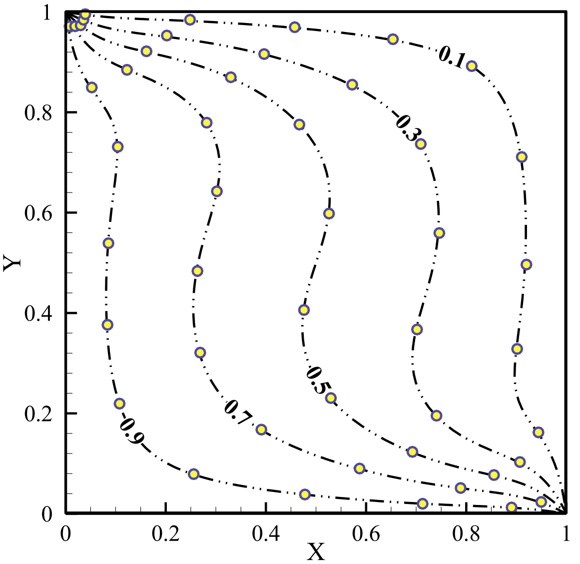

Fig. 3. Computational model validation with the numerical results [45] (present work: solid lines, and reference work: circular points).

progress of melting lines. When magnetic sources are positioned on the bottom wall, Lorentz forces are oriented in a way that leads to the strengthening of buoyancy forces and increased charge rate for the thermal storage unit. In this case, the upward shift of the central eddy leads to faster melting in the upper area of the enclosure.

Regarding the isotherms, for Case 1, as shown in Fig. 6a, isotherms become less vertical with distance from the hot wall, which indicates that convection is replacing by conduction as the dominant mode of heat transfer. As we move away from the wall, Lorentz forces get weaker, and buoyancy forces get stronger, which leads to enhanced heat convection. In Case 2 (second row of Fig. 6), vertical isotherms in the upper area of the enclosure indicate the dominance of heat conduction over convection in this area. Similar conditions but for the lower area of the enclosure is seen in Case 4 (fourth row of Fig. 6), where the concentration of magnetic field intensity is in the bottom area, which has resulted in the dominance of conduction over convection and therefore more horizontal isotherms. For Case 3, isotherms are the more vertical as they are closer to the right-side wall, especially for $Fo = 18$, which indicates that in this area conduction dominates convection.

Figs. 7 and 8 show the changes in the boundary of the melting process over time and also the volume percentage of the melt inside the enclosure. As is clear, Case 3 has the fastest melting rate. In this case, the concentration of the field intensity is farther away from the hot wall than in other cases, and this has resulted in stronger buoyancy forces near the hot wall, especially in the upper area of the enclosure, and thus accelerated melting of PCM. As shown in Fig. 8, the volume percentage of melted PCM, in this case, increases more rapidly than in other cases.

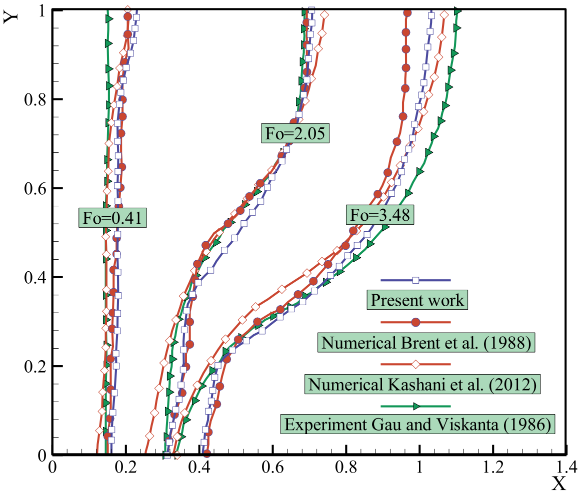

Fig. 4. Computational model validation with the numerical and experimental results [46–48].

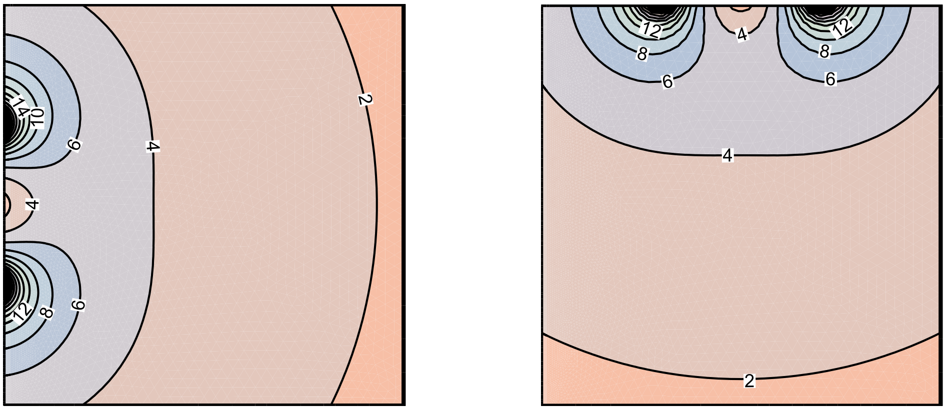

Case 1 ($Y_1 = 0.3$, $Y_1 = 0.7$ and $X_1 = X_2 = 0.05$) Case 2 ($Y_1 = Y_1 = 1.05$, $X_1 = 0.3$ and $X_2 = 0.7$)

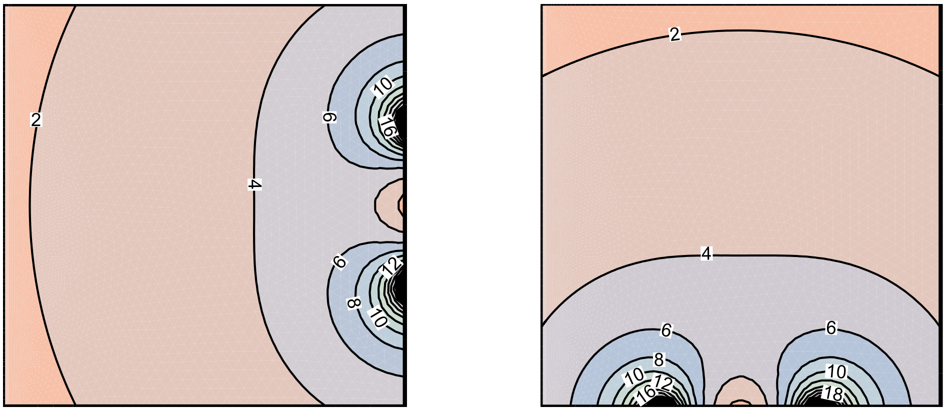

Case 3 ($Y_1 = 0.3$, $Y_1 = 0.7$ and $X_1 = X_2 = 1.05$) Case 4 ($Y_1 = Y_1 = -0.05$, $X_1 = 0.3$ and $X_2 = 0.7$)

Fig. 5. Four considered magnetic fields applied on thermal storage.

5. Conclusion

In the current study, the location influences of a pair of magnetic sources on the progress of the melting front associated with a magneto-ferro PCM in an enclosure are theoretically addressed. The left side of the enclosure is subject to the hot temperature of T_h, and the right side of the enclosure is imposed to the cold temperature of T_c. Upper and lower walls are well insulated. The pair of

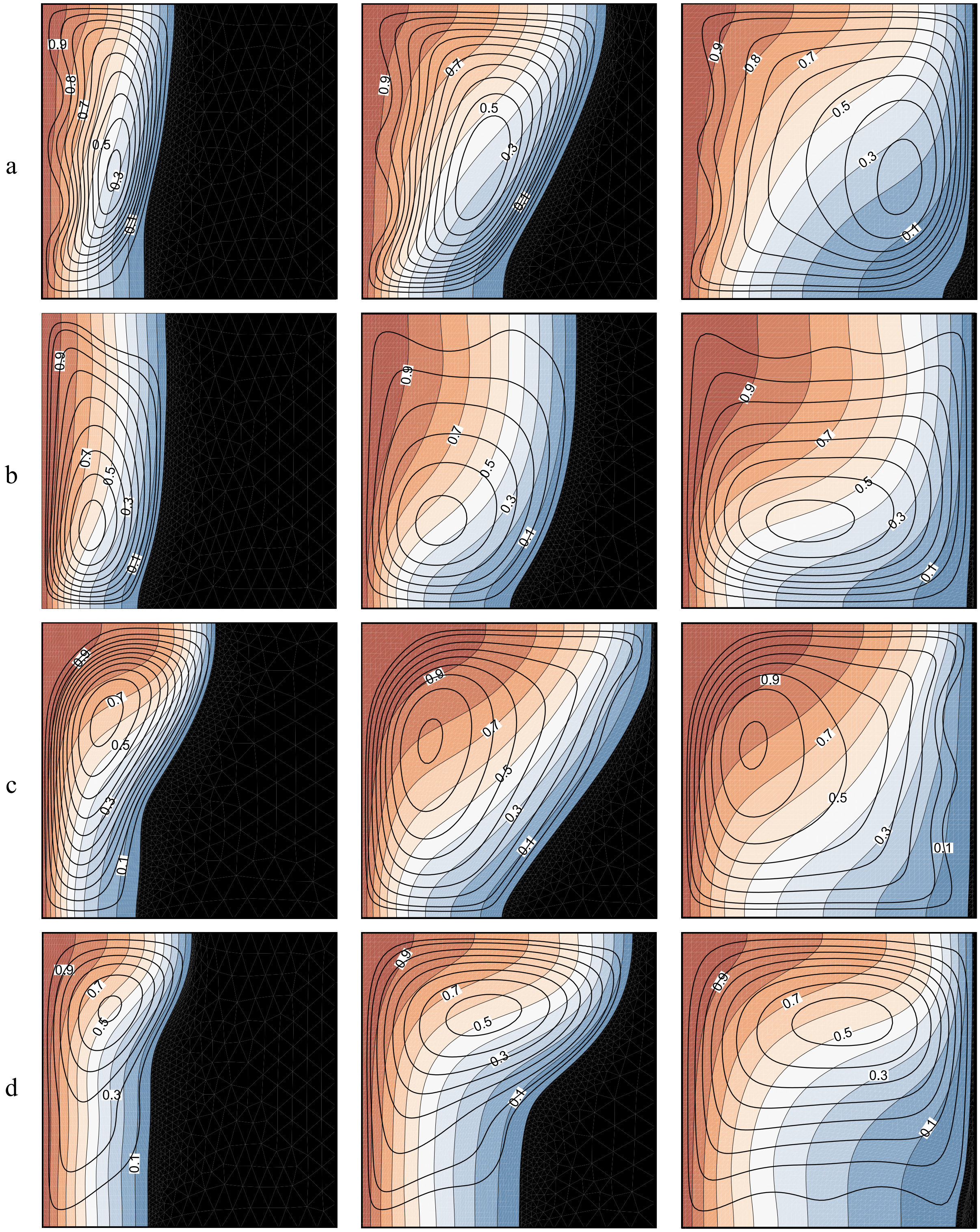

Fig. 6. development of streamlines and isothermal inside charged PCM respect to Fourier number for (a): case 1 (b): case 2 (c): case 3 (d): case 4.

magnetic sources can be placed in the vicinity of all of the walls.

The ALE deformed mesh technique is set up, which allows the deformation of the surface between the fluid and solid regions. A weighted finite element scheme, named the Galerkin method, is employed to obtain the numerical results. The grid independence test brings an optimum mesh so that it guarantees the lower run time and accurate enough results. The computational model validations

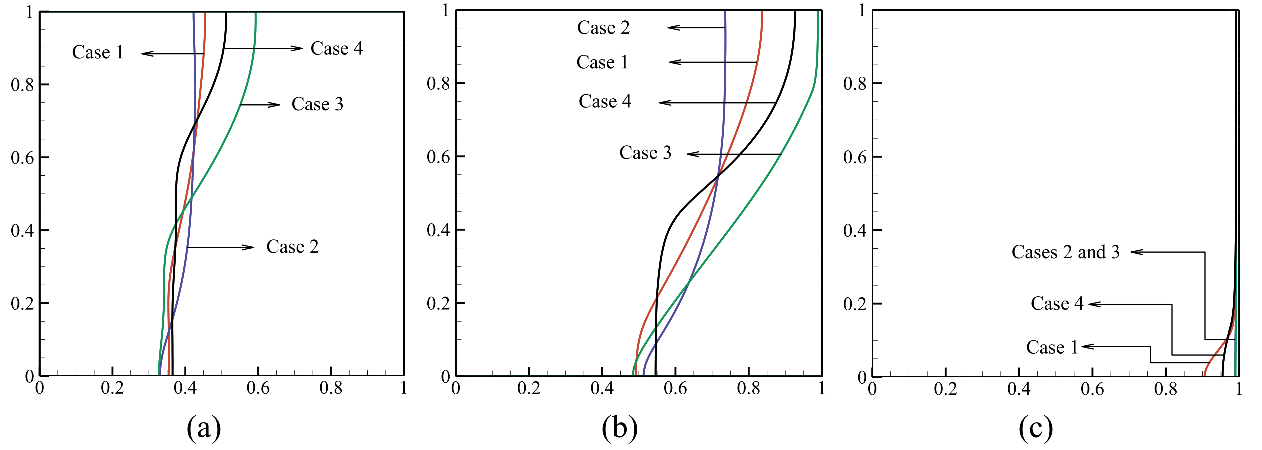

Fig. 7. melting frontier line of different cases (a) $Fo = 2$, (b) $Fo = 5$ and (c) $Fo = 18$.

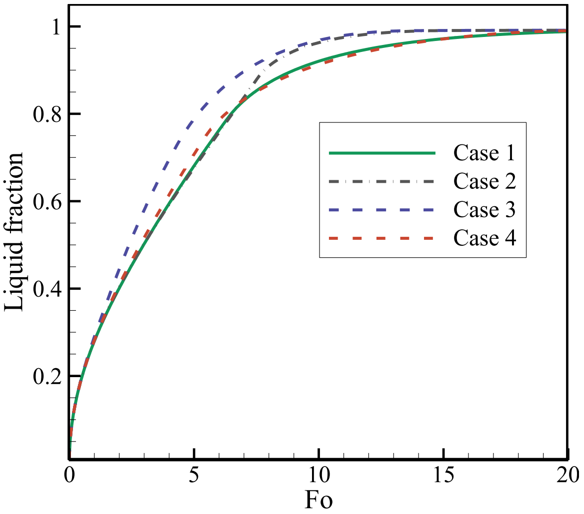

Fig. 8. Melted fraction of PCM with Fourier number.

are performed using the numerical and experimental results reported in the literature. The results manifest the dependency of the melting rate on the position of the sources. When the pair of sources are placed in the vicinity of the cold wall, the melting rate is higher. On the other hand, the final time of the melting process is almost the same for the cases with the sources placed in the adjacent of the cold left and insulated bottom walls.

Declaration of competing interests

The authors clarify that there is no conflict of interest for report.

References

[1] Z. Li, T.D. Manh, M.B. Gerdroodbary, N.D. Nam, R. Moradi, H. Babazadeh, The influence of the wedge shock generator on the vortex structure within the trapezoidal cavity at supersonic flow, Aerosp. Sci. Technol. 98 (2020) 105695.
[2] Z. Li, T.D. Manh, M.B. Gerdroodbary, N.D. Nam, R. Moradi, H. Babazadeh, The effect of sinusoidal wall on hydrogen jet mixing rate considering supersonic flow, Energy 193 (2020) 116801.
[3] Z. Li, U. Khaled, A.A. Al-Rashed, M. Goodarzi, M. Sarafraz, R. Meer, Heat transfer evaluation of a micro heat exchanger cooling with spherical carbon-acetone nanofluid, Int. J. Heat Mass Transf. 149 (2020) 119124.
[4] N.S. Bondareva, N.S. Gibanov, M.A. Sheremet, Computational study of heat transfer inside different PCMs enhanced by Al2O3 nanoparticles in a copper heat sink at high heat loads, Nanomaterials 10 (2) (2020) 284.
[5] B. Kumar, G. Seth, R. Nandkeolyar, A. Chamkha, Outlining the impact of induced magnetic field and thermal radiation on magneto-convection flow of dissipative fluid, Int. J. Therm. Sci. 146 (2019) 106101.
[6] M. Ghalambaz, S. Mehryan, E. Izadpanahi, A. Chamkha, D. Wen, MHD natural convection of Cu–Al 2 O 3 water hybrid nanofluids in a cavity equally divided into two parts by a vertical flexible partition membrane, J. Therm. Anal. Calorim. 138 (2) (2019) 1723–1743.
[7] A. Dogonchi, T. Tayebi, A.J. Chamkha, D. Ganji, Natural convection analysis in a square enclosure with a wavy circular heater under magnetic field and nanoparticles, J Therm Anal Calorim 139 (1) (2020) 661–671.
[8] T. Tayebi, A.J. Chamkha, M. Djezzar, Natural convection of CNT-water nanofluid in an annular space between confocal elliptic cylinders with constant heat flux on inner wall, Scientia Iranica 26 (5) (2019) 2770–2783.
[9] M. Ghalambaz, A.J. Chamkha, D. Wen, Natural convective flow and heat transfer of nano-encapsulated phase change materials (NEPCMs) in a cavity, Int. J. Heat Mass Transf. 138 (2019) 738–749.
[10] S. Mehryan, E. Izadpanahi, M. Ghalambaz, A. Chamkha, Mixed convection flow caused by an oscillating cylinder in a square cavity filled with Cu–Al 2 O 3/water hybrid nanofluid, J. Therm. Anal. Calorim. 137 (3) (2019) 965–982.
[11] K.A. Ayoubloo, M. Ghalambaz, T. Armaghani, A. Noghrehabadi, A.J. Chamkha, Pseudoplastic natural convection flow and heat transfer in a cylindrical vertical cavity partially filled with a porous layer, Int. J. Numer. Methods Heat Fluid Flow 30 (3) (2019) 1096–1114.
[12] A.I. Alsabery, M.A. Ismael, A.J. Chamkha, I. Hashim, Effect of nonhomogeneous nanofluid model on transient natural convection in a non-Darcy porous cavity containing an inner solid body, Int. Commun. Heat Mass Transf. 110 (2020) 104442.
[13] I. Hashim, A. Alsabery, M. Sheremet, A. Chamkha, Numerical investigation of natural convection of Al2O3-water nanofluid in a wavy cavity with conductive inner block using Buongiorno's two-phase model, Adv. Powder Technol. 30 (2) (2019) 399–414.
[14] M.S. Ishak, A.I. Alsabery, A. Chamkha, I. Hashim, Effect of finite wall thickness on entropy generation and natural convection in a nanofluid-filled partially heated square cavity, Int. J. Numer. Methods Heat Fluid Flow 30 (3) (2019) 1518–1546.
[15] M. Astanina, M. Rashidi, M. Sheremet, G. Lorenzini, Effect of porous insertion on convective energy transport in a chamber filled with a temperature-dependent viscosity liquid in the presence of a heat source term, Int. J. Heat Mass Transf. 144 (2019) 118530.
[16] A. Abhat, Low temperature latent heat thermal energy storage: heat storage materials, Sol. Energy 30 (4) (1983) 313–332.
[17] C.-.J. Ho, K. Lin, Outward melting in a cylindrical annulus, J. Energy Resour. Technol. 108 (3) (1986) 240–245.
[18] D.K. Agarwal, A. Vaidyanathan, S.S. Kumar, Synthesis and characterization of kerosene–alumina nanofluids, Appl. Therm. Eng. 60 (1–2) (2013) 275–284.
[19] S. Tiari, S. Qiu, M. Mahdavi, Discharging process of a finned heat pipe–assisted thermal energy storage system with high temperature phase change material, Energy Convers. Manag. 118 (2016) 426–437.
[20] S. Tiari, S. Qiu, M. Mahdavi, Numerical study of finned heat pipe-assisted thermal energy storage system with high temperature phase change material, Energy Convers. Manag. 89 (2015) 833–842.

[21] L. Kumar, B. Manjunath, R. Patel, S. Prabhu, Experimental investigations on melting of lead in a cuboid with constant heat flux boundary condition at two vertical walls using infra-red thermography, Int. J. Heat Mass Transf. 68 (2014) 132–140.

[22] M. Sheikholeslami, M. Jafaryar, A. Shafee, Z. Li, Hydrothermal and second law behavior for charging of NEPCM in a two dimensional thermal storage unit, Chin. J. Phys. 58 (2019) 244–252.

[23] J. Khodadadi, S. Hosseinizadeh, Nanoparticle-enhanced phase change materials (NEPCM) with great potential for improved thermal energy storage, Int. Commun. Heat Mass Transf. 34 (5) (2007) 534–543.

[24] S.F. Hosseinizadeh, A.A.R. Darzi, F.L. Tan, Numerical investigations of unconstrained melting of nano-enhanced phase change material (NEPCM) inside a spherical container, Int. J. Therm. Sci. 51 (2012) 77–83.

[25] S. Motahar, N. Nikkam, A.A. Alemrajabi, R. Khodabandeh, M.S. Toprak, M. Muhammed, Experimental investigation on thermal and rheological properties of n-octadecane with dispersed TiO2 nanoparticles, Int. Commun. Heat Mass Transf. 59 (2014) 68–74.

[26] S. Motahar, N. Nikkam, A.A. Alemrajabi, R. Khodabandeh, M.S. Toprak, M. Muhammed, A novel phase change material containing mesoporous silica nanoparticles for thermal storage: a study on thermal conductivity and viscosity, Int. Commun. Heat Mass Transf. 56 (2014) 114–120.

[27] Z. Li, A. Shahsavar, A.A. Al-Rashed, P. Talebizadehsardari, Effect of porous medium and nanoparticles presences in a counter-current triple-tube composite porous/nano-PCM system, Appl. Therm. Eng. 167 (2020) 114777.

[28] M.S. Mahdi, H.B. Mahood, A.A. Khadom, A.N. Campbell, M. Hasan, A.O. Sharif, Experimental investigation of the thermal performance of a helical coil latent heat thermal energy storage for solar energy applications, Therm. Sci. Eng. Prog. 10 (2019) 287–298.

[29] A. Ebrahimi, M.J. Hosseini, A.A. Ranjbar, M. Rahimi, R. Bahrampoury, Melting process investigation of phase change materials in a shell and tube heat exchanger enhanced with heat pipe, Renew. Energy 138 (2019) 378–394.

[30] I. Al Siyabi, S. Khanna, T. Mallick, S. Sundaram, An experimental and numerical study on the effect of inclination angle of phase change materials thermal energy storage system, J. Energy Storage 23 (2019) 57–68.

[31] M.S. Mahdi, H.B. Mahood, A.F. Hasan, A.A. Khadom, A.N. Campbell, Numerical study on the effect of the location of the phase change material in a concentric double pipe latent heat thermal energy storage unit, Therm. Sci. Eng. Prog. 11 (2019) 40–49.

[32] M. Chen, Y. He, Q. Ye, Z. Zhang, Y. Hu, Solar thermal conversion and thermal energy storage of CuO/Paraffin phase change composites, Int. J. Heat Mass Transf. 130 (2019) 1133–1140.

[33] G. Alva, L. Liu, X. Huang, G. Fang, Thermal energy storage materials and systems for solar energy applications, Renew. Sustai. Energy Rev. 68 (2017) 693–706.

[34] S. Mehryan, M. Izadi, Z. Namazian, A.J. Chamkha, Natural convection of multi-walled carbon nanotube–Fe 3 O 4/water magnetic hybrid nanofluid flowing in porous medium considering the impacts of magnetic field-dependent viscosity, J. Therm. Anal. Calorim. 138 (2019) 1541–1555.

[35] M. Izadi, R. Mohebbi, A.A. Delouei, H. Sajjadi, Natural convection of a magnetizable hybrid nanofluid inside a porous enclosure subjected to two variable magnetic fields, Int. J. Mech. Sci. 151 (2019) 154–169.

[36] H. Sajjadi, A. Amiri Delouei, M. Izadi, R. Mohebbi, Investigation of MHD natural convection in a porous media by double MRT lattice Boltzmann method utilizing MWCNT–Fe3O4/water hybrid nanofluid, Int. J. Heat Mass Transf. 132 (2019) 1087–1104.

[37] S.A.M. Mehryan, M.A. Sheremet, M. Soltani, M. Izadi, Natural convection of magnetic hybrid nanofluid inside a double-porous medium using two-equation energy model, J. Mol. Liq. 277 (2019) 959–970.

[38] T. Armaghani, A. Kasaeipoor, M. Izadi, I. Pop, MHD natural convection and entropy analysis of a nanofluid inside T-shaped baffled enclosure, Int. J. Numer. Methods Heat Fluid Flow 28 (12) (2018) 2916–2941.

[39] S. Mehryan, M. Izadi, A.J. Chamkha, M.A. Sheremet, Natural convection and entropy generation of a ferrofluid in a square enclosure under the effect of a horizontal periodic magnetic field, J. Mol. Liq. 263 (2018) 510–525.

[40] J.C. Umavathi, S. Mohiuddin, M.A. Sheremet, MHD flow in a vertical channel under the effect of temperature dependent physical parameters, Chin. J. Phys. 58 (2019) 324–338.

[41] S.A.M. Mehryan, A. Tahmasebi, M. Izadi, M. Ghalambaz, Melting behavior of phase change materials in the presence of a non-uniform magnetic-field due to two variable magnetic sources, Int. J. Heat Mass Transf. 149 (2020) 119184.

[42] M. Ghalambaz, S.M. Hashem Zadeh, S.A.M. Mehryan, I. Pop, D. Wen, Analysis of melting behavior of PCMs in a cavity subject to a non-uniform magnetic field using a moving grid technique, Appl. Math. Model. 77 (2020) 1936–1953.

[43] M. Ghalambaz, S.M. Hashem Zadeh, S.A.M. Mehryan, K. Ayoubi Ayoubloo, N. Sedaghatizadeh, Non-Newtonian behavior of an electrical and magnetizable phase change material in a filled enclosure in the presence of a non-uniform magnetic field, Int. Commun. Heat Mass Transf. 110 (2020) 104437.

[44] The finite element method for fluid dynamics, in: O.C. Zienkiewicz, R.L. Taylor, P. Nithiarasu (Eds.), The Finite Element Method for Fluid Dynamics (Seventh Edition), Butterworth-Heinemann, Oxford, 2014pp. iii.

[45] M. Sathiyamoorthy, A.J. Chamkha, Natural convection flow under magnetic field in a square cavity for uniformly (or) linearly heated adjacent walls, Int. J. Numer. Methods Heat Fluid Flow 22 (5) (2012) 677–698.

[46] C. Gau, R. Viskanta, Melting and solidification of a pure metal on a vertical wall, J. Heat Transf. 108 (1) (1986) 174–181.

[47] S. Kashani, A. Ranjbar, M. Abdollahzadeh, S. Sebti, Solidification of nano-enhanced phase change material (NEPCM) in a wavy cavity, Heat Mass Transf. 48 (7) (2012) 1155–1166.

[48] A. Brent, V. Voller, K. Reid, Enthalpy-porosity technique for modeling convection-diffusion phase change: application to the melting of a pure metal, Numer. Heat Transf. Part A Appl. 13 (3) (1988) 297–318.